Infrared Dielectric Anisotropy and Phonon Modes of Rutile TiO2

Rafal Korlacki
University of Nebraska-Lincoln, rkorlacki2@unl.edu

Stefan Schöche
University of Nebraska-Lincoln

Tino Hofmann
University of Nebraska-Lincoln

Tom E. Tiwald
J. A. Woollam Co.

Mathias Schubert
University of Nebraska-Lincoln, schubert@engr.unl.edu

Infrared dielectric anisotropy and phonon modes of rutile TiO2

S. Schöche, T. Hofmann, R. Korlacki, T. E. Tiwald, and M. Schubert

Additional information on J. Appl. Phys.

Infrared dielectric anisotropy and phonon modes of rutile TiO$_2$

S. Schöche,[1,a)] T. Hofmann,[1] R. Korlacki,[1] T. E. Tiwald,[2] and M. Schubert[1]
[1]*Department of Electrical Engineering, Center for Nanohybrid Functional Materials, University of Nebraska-Lincoln, Nebraska 68588-0511, USA*
[2]*J.A. Woollam Co., Inc. 645 M Street, Suite 102, Lincoln, Nebraska 68508, USA*

Spectroscopic ellipsometry in the mid-infrared and far-infrared spectral range and generalized ellipsometry in the mid-infrared spectral range are used to investigate the anisotropic dielectric response of rutile TiO$_2$. The ordinary and extraordinary dielectric function tensor components and all infrared active phonon mode parameters of single crystalline rutile TiO$_2$ are determined with high accuracy for wavelengths from 3 μm to 83 μm. The data were acquired from samples of (001), (100), and (111) surfaces cut from bulk single crystals. A factorized model dielectric function is employed in order to determine the frequencies and damping parameters of the transverse and longitudinal phonon modes with A_{2u} and E_u symmetries. The bands of total reflection of s- and p-polarized light in dependence of the angle of incidence for highly symmetric sample cuts and orientations are derived. Excellent agreement with phonon modes reported in literature is obtained. Introduction of two additional modes for ordinary as well as extraordinary component of the dielectric function tensor was necessary to most accurately match the experimental data. The spectral position of the additional modes is compared to the calculated phonon density of states. The low-frequency dielectric constants are calculated from the determined phonon mode parameters and the high-frequency dielectric constants by applying the Lyddanne-Sachs-Teller relation. The presented data revise existing infrared optical function data and will be suitable for interpretation of any kind of infrared spectra for bulk TiO$_2$ single crystal substrates, thin films, and TiO$_2$ nanostructures. © *2013 AIP Publishing LLC*. [http://dx.doi.org/10.1063/1.4802715]

I. INTRODUCTION

For over half a century, rutile TiO$_2$ was intensively studied by theorists and experimental scientists due to interesting physical properties, such as high static dielectric constant and large uniaxial refractive index. It was used as an example material to study phonon mode behavior in metal oxides and the anisotropic dielectric function (DF) in the range of electronic band-to-band transitions in uniaxial materials. Early applications included optical devices made from bulk crystals like compensators, polarizers, or traveling wave masers.[1–3] Modern applications of TiO$_2$ include high-k dielectrics in semiconductor transistors,[4] optical coatings,[5] and photocatalysts in dye-sensitized solar cells,[6] amongst other.[7] Even though being studied intensively, there are still properties of rutile TiO$_2$ not understood completely. For correlation of theoretical model predictions with material properties and analysis of phonon mode properties of thin films grown on TiO$_2$ substrates, accurate knowledge of the infrared (IR) dielectric function and phonon mode parameters of TiO$_2$ is required. Existing DF data for the long-wavelength spectral region are available only in tabulated form and mostly obtained from Kramers-Kronig (K-K) inverted reflectivity spectra, which lack in precession and accuracy compared to an analysis of spectroscopic ellipsometry (SE) data measured directly at wavelengths of interest.

First experiments to investigate the phonon mode properties of rutile TiO$_2$ in the far-IR spectral region were carried out by Spitzer *et al.*[8] The authors determined the DF of a (001)-oriented rutile TiO$_2$ sample by K-K inversion but did not report a parameterization of the DF, for example, by applying a classical harmonic oscillator approach (HOA). Gervais and Piriou demonstrated that a simple, four-parameter semiquantum model (FPSQ) suffices to correctly model the experimental data given by Spitzer *et al.*[9] Motivated by anharmonic quantum theories, this model theorizes independent damping parameters for each longitudinal optical (LO) and transverse optical (TO) phonon mode to account for anharmonic broadening effects in crystals of multiple (polar) phonon-modes. Gervais and Piriou applied their model to calculate the ordinary and extraordinary DF from K-K inverted IR-reflectivity spectra of c-plane corundum Al$_2$O$_3$, rutile TiO$_2$, and α-SiO$_2$ and rejected the harmonic oscillator approach for materials with broad phonon bands.[9–11] Additionally to IR reflectometry measurements, Raman spectroscopy and neutron scattering experiments were performed to determine the phonon mode frequencies.[12–14] Traylor *et al.* applied various forms of rigid-ion and shell models to fit their experimental neutron diffraction data for the whole Brillouin zone.[13] Theorists later predicted several models to calculate the phonon mode properties of rutile TiO$_2$ by applying density functional theory, plane-wave pseudo-potential formalisms, and other theories. An overview over existing theoretical studies can be found, for example, in the recent paper by Mitev *et al.*[15] The pressure and temperature dependence of the high, anisotropic low-frequency dielectric constant ε$_0$ was studied by capacitance measurements in the kHz frequency range[14,16]

and in microwave waveguides and resonators in the GHz frequency range.[3,17,18] The anisotropic optical properties in the near-IR to visible spectral range were first investigated by DeVore[1] and Cronemeyer.[2,19] The authors determined the ordinary and extraordinary refractive index from minimum deviation measurements on prisms[1,19] and reflectivity measurements on different surface cuts of a rutile TiO_2 sample.[2,19] Jellison *et al.* and Schubert *et al.* used rutile TiO_2 samples to demonstrate the capability of generalized ellipsometry to accurately determine the DF tensor components and orientation of the optical axis in uniaxial materials in the visible to ultraviolet spectral range.[20,21] Tiwald and Schubert extended the measured spectral range from the mid-IR to the vacuum-ultraviolet (0.148 to 33 μm).[22] Their tabulated data corroborate the results of the anisotropic DF tensor components found for the near-IR spectral range by DeVore and for the visible to ultraviolet spectral range by Jellison *et al.* In the mid-IR spectral range, the DF data match the ordinary component determined by Gervais and Piriou, while there is significant mismatch between the reported extraordinary components. Schubert *et al.* applied the FPSQ model proposed by Gervais and Piriou to revise the IR DF tensor components of corundum Al_2O_2.[23] The authors demonstrated that SE is an excellent technique to determine the IR DF of anisotropic materials avoiding inaccuracies due to extrapolation into experimentally inaccessible spectral regions as required for K-K analysis of reflectivity data. Further, Schubert *et al.* derived a general rule for the phonon broadening parameters, necessary to assure a positive imaginary part and thus physical meaning of the DF.

In this paper, we apply spectroscopic ellipsometry in the mid-IR and far-IR spectral range and generalized ellipsometry in the mid-IR spectral range to investigate the anisotropic dielectric response of rutile TiO_2. Experimental data for wavelengths from 3 μm to 83 μm are acquired for samples of (001), (100), and (111) surface orientation cut from a bulk single crystal. The FPSQ model is used to determine all IR-active longitudinal and transverse optical phonon mode parameters of rutile TiO_2 in a model analysis of experimental data taken in the standard ellipsometry mode for highly symmetric orientations of the (001) and (100)-oriented samples. The determined phonon mode frequencies are utilized to calculate the bands of total reflection of *p*- and *s*-polarized light for these highly symmetric sample orientations in dependence of the angle of incidence. The *p*- and *s*-reflection coefficients spectra for the experimental angle of incidence of 72° are calculated to guide the reader in understanding the spectral features in the ellipsometry data. Second-derivative spectra of the pseudo-dielectric function illustrate critical-point-like structures in the reststrahlen range for the highly symmetric sample orientations. The derived best-matching model is used without further regression analysis to determine the Euler angles for a rutile TiO_2-(111)-sample of arbitrary *c*-axis orientation. Excellent match between experimental and model calculated generalized ellipsometry data for all four measured sample orientations proves the quality of our dielectric function model. Two additional phonon modes each, for ordinary and extraordinary dielectric function tensor component, were introduced to best-match the

experimental data. Signatures of these symmetry-forbidden modes were found for all investigated surface cuts. The spectral position of these modes is compared to the calculated phonon density of states (DOS) to narrow down the possible origin of the additional modes. The real and imaginary part of the material dielectric function of rutile TiO_2 as determined from the model analysis and a point-by-point fit are found in excellent agreement. The dielectric loss function as extracted from the model analysis is presented. A comparison of the determined phonon mode parameters frequency, broadening, high-frequency dielectric constants ε_∞ and low-frequency dielectric constants ε_0 with reported values shows our results in context of existing literature. The resulting optical constants are given to revise the existing data. These optical constants will be useful for IR analysis of heterostructures deposited on bulk TiO_2 single crystal substrates as well as TiO_2 thin films and nanostructures.

II. EXPERIMENT

Spectroscopic ellipsometry measurements at room temperature were carried out on a set of synthetic, single crystal uniaxial rutile TiO_2 samples of different surface orientations cut from the same bulk crystal. The nominal surface orientations of the samples investigated here were (001) (*c*-plane), (100) (*a*-plane), and (111). Crystal orientations were confirmed by Laue backscattering and polarization microscopy. The lattice constants for all samples were determined from x-ray diffraction analysis to be $a = b = 4.492$ Å and $c = 2.893$ Å. The *c*-axis inclination angles from the surface normal were determined to be 0° (*c*-plane sample), 90° (*a*-plane sample), and 42° ((111)-oriented sample) with uncertainties of 3°. All samples were one-side polished to avoid backside reflections in the ellipsometry measurements. The sample thicknesses were approximately 350 μm.

The mid-IR measurements were carried out in the spectral range from 300 cm^{-1} to 6000 cm^{-1} using a commercial IR ellipsometer (J.A. Woollam Co., Inc.). A custom-built far-IR rotating analyzer ellipsometer was used to perform measurements in the spectral range from 100 cm^{-1} to 650 cm^{-1}. A spectral resolution of 1 cm^{-1} was chosen for both Fourier transform-based instruments. The experimental data sets taken on the two instruments match nearly perfectly in the overlapping spectral region.

Highly symmetric sample orientations were chosen for the data acquisition on the *c*-plane and *a*-plane samples. For the *c*-plane sample, the *c*-axis is oriented parallel to the surface normal. For the *a*-plane sample, the *c*-axis was either oriented parallel ($c \parallel x$) or perpendicular to the plane of incidence ($c \perp x$). Measurements on the (111) sample were performed at four different in-plane orientations. Between the measurements, the sample was rotated manually by approximately 45°.

III. THEORY

Rutile TiO_2 crystallizes in a tetragonal unit cell causing uniaxial birefringence with the optical axis oriented along the crystal *c*-axis. Group theory predicts three distinct IR-active phonon modes for rutile TiO_2 with dipole-moment

oscillation perpendicular (electric field vector $\mathbf{E} \perp c$, E_u) and one mode with dipole-moment oscillation parallel to the c-axis ($\mathbf{E} \parallel c$, A_{2u}).[24] These phonon modes split into LO and TO modes due to Coulomb interaction.[25] Resonant excitation of the phonons by the IR spectroscopic ellipsometry probe beam strongly affects the state of polarization of the reflected beam, thereby providing high sensitivity to the lattice properties. For analysis of the ellipsometry data, model calculations are performed during which significant model parameters are varied until experimental and model calculated data match as close as possible.[26]

A. Ellipsometry equations

The standard ellipsometry parameters Ψ and Δ are defined by the ratio ρ of the complex valued Fresnel reflection coefficients[27]

$$\rho = \frac{r_p}{r_s} = \tan \Psi \exp(\mathrm{i}\Delta). \qquad (1)$$

The sample surface (x-y plane) and the sample normal span a right-handed $\{x, y, z\}$ laboratory coordinate system with the origin set to the sample surface and x axis parallel to the plane of incidence, which is defined by the incident and reflected light beam.[28] The polarization states s and p refer to light polarized perpendicular and parallel to this plane of incidence, respectively. A common representation of Ψ and Δ is the pseudo-DF $\langle \epsilon \rangle$, which formally converts the standard ellipsometry parameters into virtual bulk material DF values assuming a two phase model (air-substrate)[26,27]

$$\langle \epsilon \rangle = \left[\left(\frac{1-\rho}{1+\rho} \right)^2 \sin^2 \Phi_a + \cos^2 \Phi_a \right] \tan^2 \Phi_a, \qquad (2)$$

where Φ_a is the angle of incidence. The pseudo-DF is equivalent to the material DF only in the case of a single isotropic bulk layer with perfectly smooth surface. For birefringent materials or if overlayers are present, a model analysis is required to relate the pseudo-DF to the material properties. However, a formal transformation of Ψ and Δ into $\langle \epsilon \rangle$ is always possible for a standard ellipsometry measurement.

For anisotropic bulk materials, the ellipsometry measurement depends on the principal axis DF values $\varepsilon_x, \varepsilon_y, \varepsilon_z$, the orientation of the crystal axis with respect to the plane of incidence, and the polarization state of the incident light beam. For high-symmetry orientations of birefringent bulk materials, i.e., the principal crystal axes coincide with the laboratory coordinate system $\{x, y, z\}$, no mode conversion of s-polarized light to p-polarized light and vice versa occurs and a single ratio of complex reflection coefficients as given by Eq. (1) is sufficient to characterize the experiment (standard ellipsometry). The p and s reflection coefficients in this situation are[29]

$$r_p = \frac{N_{xa} - N_{az}}{N_{az} + N_{xa}}, \qquad (3)$$

$$r_s = \frac{N_{aa} - N_{yy}}{N_{aa} + N_{yy}}, \qquad (4)$$

with

$$N_{ij} = \sqrt{\varepsilon_i} \sqrt{1 - \frac{\varepsilon_a}{\varepsilon_j} \sin^2 \Phi_a}. \qquad (5)$$

The index a refers to the DF ε_a of the ambient medium, which in our situation is unity for air. For a uniaxial material, the DF tensor in the sample coordinate system is given by the diagonal tensor

$$\varepsilon = \begin{pmatrix} \varepsilon_\perp & 0 & 0 \\ 0 & \varepsilon_\perp & 0 \\ 0 & 0 & \varepsilon_\parallel \end{pmatrix} \qquad (6)$$

with only two different components $\varepsilon_\perp$ and $\varepsilon_\parallel$, where "$\perp$" and "$\parallel$" denote polarization perpendicular and parallel to the c-axis, respectively. The tensor in the given form applies if the sample coordinate system and laboratory coordinate system coincide, i.e., the c-axis is oriented parallel to the sample surface normal. Other highly symmetric sample orientations are described by permutations of the diagonal elements.

In all situations, for which the crystal c-axis does not coincide with an axis of the laboratory coordinate system, mode conversion between s and p polarized light occurs upon reflection from the sample surface and the generalized ellipsometry approach has to be applied.[20,28–30] In the Jones matrix formalism, the interaction of light with a sample is described by the Jones matrix $\mathbf{J}$ that connects the incoming Jones vector with the reflected Jones vector[20,28–30]

$$\begin{pmatrix} E_{rp} \\ E_{rs} \end{pmatrix} = \mathbf{J} \begin{pmatrix} E_{ip} \\ E_{is} \end{pmatrix} = \begin{pmatrix} r_{pp} & r_{ps} \\ r_{sp} & r_{ss} \end{pmatrix} \begin{pmatrix} E_{ip} \\ E_{is} \end{pmatrix}, \qquad (7)$$

where $E_{s,p}$ refers to the electric field component perpendicular and parallel to the plane of incidence, respectively. In analogy to the standard ellipsometry case, the generalized ellipsometry parameters are described by three ratios of the polarized-light reflection coefficients r_{ij}:[20,28–30]

$$R_{pp,ps,sp} = \frac{r_{pp,ps,sp}}{r_{ss,pp,ss}} = \tan \Psi_{pp,ps,sp} \exp(\mathrm{i}\Delta_{pp,ps,sp}). \qquad (8)$$

The reflection coefficients r_{ij} can be calculated by applying a 4×4 transfer matrix formalism for which the DF tensor components are used as input parameters. To account for the orientation of the material relative to the laboratory coordinate system, a coordinate transformation using the Euler angles $\{\varphi, \theta, \psi\}$ is necessary. The dielectric function tensor in the laboratory coordinate system is given by[27]

$$\varepsilon = \begin{pmatrix} \varepsilon_{xx} & \varepsilon_{xy} & \varepsilon_{xz} \\ \varepsilon_{yx} & \varepsilon_{yy} & \varepsilon_{yz} \\ \varepsilon_{zx} & \varepsilon_{zy} & \varepsilon_{zz} \end{pmatrix} = \mathbf{A} \begin{pmatrix} \varepsilon_\perp & 0 & 0 \\ 0 & \varepsilon_\perp & 0 \\ 0 & 0 & \varepsilon_\parallel \end{pmatrix} \mathbf{A}^T \qquad (9)$$

with $\mathbf{A}(\varphi, \theta, \psi)$ being a rotation matrix. For arbitrary orientation of the c-axis in an uniaxial sample, φ represents the angle between the projection of the c-axis on the sample surface (x–y plane) and the x-axis. The angle θ is equivalent to the tilt of the c-axis from the sample surface normal. The angle ψ describes a rotation around the resulting c-axis after

applying the first two rotations and does not change the DF tensor for a uniaxial material since there are only two independent DF tensor components in the principal axis coordinate system. In order to determine a unique set of DF tensor components, measurements at different in-plane sample orientations (φ) are required.

The DF tensor components can be given as tabulated values for each wavelength or can be modeled by using parameterized, wavelength-dependent algebraic functions, so-called model dielectric functions (MDF). These MDF describe a specific physical process in the material such as a lattice vibration or an electronic interband transition[31] and are combined in order to render the overall spectral shape of a material's DF. A detailed description of the MDF approach applied here is given in Sec. III B.

A regression analysis (Levenberg-Marquardt algorithm) is performed, during which the model parameters are varied until calculated and experimental data match as close as possible.[31] This is done by minimizing the mean square error function (χ^2), which is weighed to estimated experimental errors (σ). For standard ellipsometry, $\chi^2_{\text{St-SE}}$ is calculated by[32]

$$\chi^2_{\text{St-SE}} = \frac{1}{2S-K} \sum_{i=1}^{S} \left[\left(\frac{\Psi_i - \Psi_i^c}{\sigma_i^{\Psi}} \right)^2 + \left(\frac{\Delta_i - \Delta_i^c}{\sigma_i^{\Delta}} \right)^2 \right], \quad (10)$$

where the index i indicates the calculated (Ψ_i^c, Δ_i^c) and experimental (Ψ_i, Δ_i) data pairs at photon energy E_i for a total of S single photon energies and K denotes the total number of real valued parameters that are varied during the regression analysis. Accordingly, a weighed mean squared error function χ^2_{GE} for the generalized ellipsometry case can be defined by adding the according terms for $\Psi_{ps,sp}$ and $\Delta_{ps,sp}$.

B. Infrared model dielectric function

The infrared response at photon energy $\hbar\omega$ of a solid crystalline media with multiple (l) polar-optical phonon modes is commonly described by damped harmonic oscillator functions for each IR-active phonon branch (HOA)[33]

$$\varepsilon(\omega) = \varepsilon_{\infty} + \sum_{j}^{l} \frac{4\pi F_{\text{TO}i}\omega_{\text{TO}i}^2}{\omega_{\text{TO}i}^2 - \omega^2 - i\Gamma_{\text{TO}\omega}}, \quad (11)$$

where $F_{\text{TO}i}$, $\Gamma_{\text{TO}i}$, and $\omega_{\text{TO}i}$ are strength, broadening, and resonance energy of the ith TO-phonon and ε_{∞} is the high-frequency dielectric constant. Gervais and Piriou pointed out that different phonon decay times should be considered for LO and TO phonons for multiple phonon-mode crystals of large TO-LO splitting.[10,33] However, the HOA does not allow independent broadening for TO and LO phonons. Motivated by anharmonic quantum theories, Gervais and Piriou derived and successfully applied a FPSQ model that theorizes independent damping parameters for each LO and TO phonon mode to account for anharmonic effects in multiple (polar) phonon-mode crystals,[9,10,33]

$$\varepsilon(\omega) = \varepsilon_{\infty} \prod_{i}^{j} \frac{\omega^2 + i\gamma_{\text{LO}i}\omega - \omega_{\text{LO}i}^2}{\omega^2 + i\gamma_{\text{TO}i}\omega - \omega_{\text{TO}i}^2}. \quad (12)$$

In this highly symmetric form, the DF ε and dielectric loss function ε^{-1} can easily be evaluated. The energies $\omega_{\text{TO}i}$ are the poles of the DF, while the energies $\omega_{\text{LO}i}$ are given by the poles of the dielectric loss function.

Symmetry-forbidden phonon modes can occur, if the sample is not a perfect single crystal. These modes can, for example, be related to a specific defect (impurity modes) or bound to surfaces and interfaces between substrate and a thin film. In this paper, additional modes are accounted for by adding an additional term to the product in Eq. (12). Typically, these modes show small TO-LO splitting and large broadening values. The general rule that $\omega_{\text{TO},i} < \omega_{\text{LO},i} < \omega_{\text{TO},i+1}$ applies also for these additional modes. Therefore, depending on the spectral position of the additional mode, $\omega_{\text{TO}}^{\text{AM}}$ can be larger or smaller than $\omega_{\text{LO}}^{\text{AM}}$.

Gervais and Piriou pointed out that the conditions found by Lowndes, $\gamma_{\text{LO}i} > \gamma_{\text{TO}i}$ and $\gamma_{\text{LO}i}/\gamma_{\text{TO}i} \geq (\omega_{\text{LO}i}/\omega_{\text{TO}i})^2$, must be satisfied in order to keep the physical meaning of ε, i.e., positive extinction coefficients.[9] Schubert *et al.* pointed out that these conditions are only valid for a single phonon mode pair and derived a generalized Lowndes condition,[23]

$$\sum_{i}^{l}(\gamma_{\text{LO}i} - \gamma_{\text{TO}i}) \overset{!}{\geq} 0, \quad (13)$$

i.e., for some of the phonon mode pairs, γ_{TO} is allowed to exceed γ_{TO} as, e.g., observed for sapphire.[23] The static dielectric constant is related to the high-frequency dielectric constant by the Lyddanne-Sachs-Teller (LST) relation[34,35]

$$\varepsilon_0 = \varepsilon_{\infty} \prod_{i}^{l} \frac{\omega_{\text{LO}i}^2}{\omega_{\text{TO}i}^2}. \quad (14)$$

C. Bands of total reflection in anisotropic materials

Total reflection occurs for wavelengths near optical lattice resonance frequencies, the so-called reststrahlen bands. At total reflection, $|r_p|^2$ and/or $|r_s|^2$ equal unity. A simple rule for identifying bands of total reflection for samples of high-symmetry surface cuts can be obtained by inspecting the p- and s-polarized reflection coefficients. From the condition $|r_p|^2 = 1$ in Eq. (3), it follows that total reflection occurs for p-polarized light when

$$\text{Re}\left\{ \sqrt{\varepsilon_x^*} \left(1 - \frac{\sin^2 \Phi_a}{\varepsilon_z} \right)^{1/2} \right\} = 0, \quad (15)$$

where Re{ } denotes the real part of a complex quantity. This condition is fulfilled if (a) $\varepsilon_x < 0$ and $(\sin^2 \Phi_a/\varepsilon_z) < 1$ or if (b) $\varepsilon_x > 0$ and $(\sin^2 \Phi_a/\varepsilon_z) > 1$. It is convenient to introduce the quantity ω_{LO^*} defined as those frequencies for which the DF equals the square of the x component of the wavevector $k_x^2 = (n_a \sin \Phi_a)^2$, i.e., $\varepsilon_j(\omega_{\text{LO}^*j,i}) = \sin^2 \Phi_a$ with $j = x, y, z$ for the ith LO phonon mode. Note that $\omega_{\text{LO}^*i} \geq \omega_{\text{LO}i}$ and $\omega_{\text{LO}^*i} = \omega_{\text{LO}i}$ at $\Phi_a = 0$. For case (a), the incident photon energy ω must be within a spectral range for which ε_x is negative, i.e. $\omega = \{\omega_{\text{TO}}, \omega_{\text{LO}}\}_{x,i}$ while ω is outside the LO-frequency ranges $\{\omega_{\text{LO}}, \omega_{\text{LO}^*}\}_{z,k}$. In intersections of both

frequency ranges, the condition for total reflection is abandoned due to dielectric loss along z. Case (b) is fulfilled when ω is within $\{\omega_{LO}, \omega_{LO^*}\}_{z,i}$ but not within $\{\omega_{TO}, \omega_{LO}\}_{x,k}$. All p-polarized reflection conditions for multiple-phonon-mode crystals are obtained by the sum of exclusive intersections between the frequency sets $\{\omega_{TO}, \omega_{LO}\}_{x,i}$ and $\{\omega_{LO}, \omega_{LO^*}\}_{z,k}$

$$\omega \in \bigcup_{i,k}^{l,m} \{\omega_{TO}, \omega_{LO}\}_{x,i} \setminus \{\omega_{LO}, \omega_{LO^*}\}_{z,k}, \qquad (16)$$

where i and k run over all l, m phonon branches, which are active in ε_x and ε_z, respectively. Note that unless ε_x equals ε_z, the p-polarized reflectivity contains sharp spectral cutoffs or insets at frequencies near LO phonons along both directions, x and z, and allows for immediate experimental access to the LO-phonon frequencies. For isotropic materials, no specific features occur in the reststrahlen spectra near LO phonon frequencies.

The s-polarized bands of total reflection are related to ε_y only. From the condition $|r_s|^2 = 1$ in Eq. (4), it follows that total reflection occurs for s-polarized light when

$$\mathrm{Re}\left\{ \sqrt{\varepsilon_y^*}\left(1 - \frac{\sin^2 \Phi_a}{\varepsilon_y}\right)^{1/2} \right\} = 0, \qquad (17)$$

which is satisfied if (a) $\varepsilon_y < 0$ and $(\sin^2\Phi_a/\varepsilon_y) < 1$ or if (b) $\varepsilon_y > 0$ and $(\sin^2\Phi_a/\varepsilon_y) > 1$. Similar to the cases for p-polarized light, total reflection of s-polarized light occurs in the unified spectral ranges $\{\omega_{TO}, \omega_{LO}\}_{y,i}$ and $\{\omega_{LO}, \omega_{LO^*}\}_{y,i}$,

$$\omega \in \bigcup_i^n \{\omega_{TO}, \omega_{LO^*}\}_{y,i}. \qquad (18)$$

The sum has to be taken over all n IR-active phonon mode branches for polarization parallel y resulting in n bands of total s-reflection. Table I summarizes the conditions for total reflection of p- and s-polarized light for the highly symmetric sample orientations of rutile TiO_2 investigated in this study.

IV. RESULTS AND DISCUSSION

The experimental data of the c-plane and a-plane samples measured in the standard ellipsometry mode at highly symmetric orientation was analyzed in a multi-sample

analysis, where the same set of parameters for the MDF is applied for each data set to simultaneously minimize the weighed error function χ^2 in order to increase sensitivity for all parameters of each phonon mode of E_u- and A_{2u}-symmetry. Figure 1 shows the experimental (symbols) and best-matching model calculated data (solid lines) of the ellipsometric parameters Ψ and $\cos\Delta$ at an angle of incidence Φ_a of 72° for the c-plane rutile TiO_2 surface over the whole measured spectral range from the far-IR to mid-IR. Note the overlap of the experimental data points determined on the custom-built far-IR ellipsometer and the commercial mid-IR
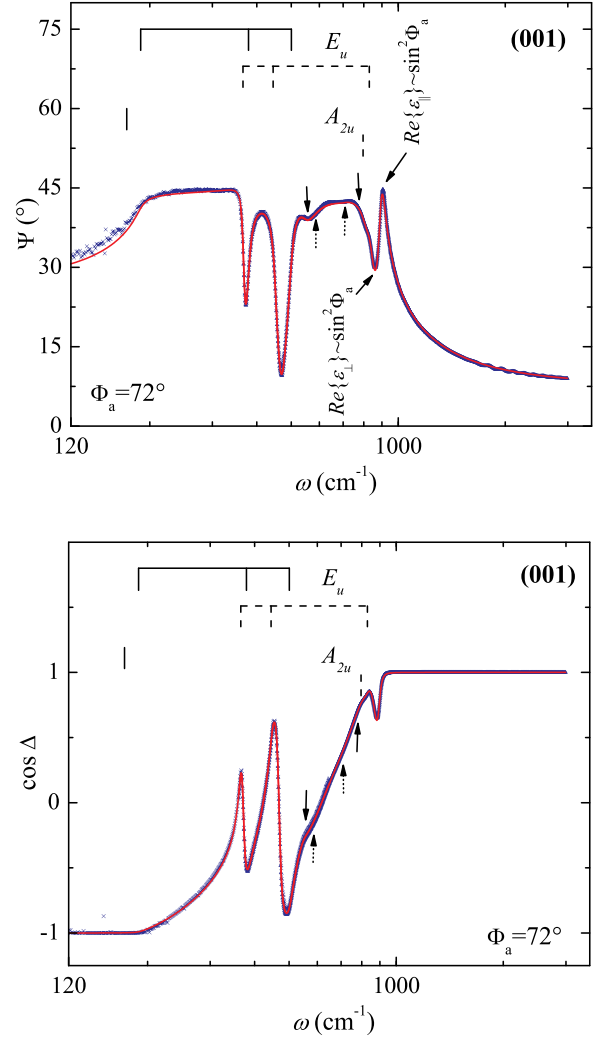

FIG. 1. Experimental (symbols) and best-match model calculated data (solid lines) of the ellipsometric parameters Ψ and $\cos\Delta$ for c-plane rutile TiO_2. Very good agreement between experimental and best-match model calculated data was achieved by applying the factorized MDF in Eq. (12). The energetic position of transverse and longitudinal phonon modes of E_u- and A_{2u}-symmetry is indicated by brackets (solid brackets: TO phonons; dashed brackets: LO phonons). Two additional modes needed to be included for each component of the dielectric function tensor in order to achieve the excellent match between experimental and model data in the spectral range between $500\,\mathrm{cm}^{-1}$ and $800\,\mathrm{cm}^{-1}$. Their energetic position is indicated by arrows (solid arrows: additional modes in $\varepsilon_\perp$; dotted arrows: additional modes in $\varepsilon_\parallel$). $\varepsilon_\parallel$ and $\varepsilon_\perp$ approach unity at different energies above the reststrahlen bands. The loss in p- and s-reflectivity causes the derivative-like structure in Ψ near $900\,\mathrm{cm}^{-1}$. Note the nearly indistinguishable overlap of the experimental data points determined on the custom-built far-IR ellipsometer and the commercial mid-IR ellipsometer in the spectral range between $300\,\mathrm{cm}^{-1}$ and $650\,\mathrm{cm}^{-1}$.

TABLE I. Bands of total reflection in r_p and r_s for high-symmetry orientations of rutile TiO_2. The frequencies ω_{LO^*} are defined by $\varepsilon(\omega_{LO^*})_{\perp,\parallel} = n_a^2 \sin^2\Phi_a$. Total reflection occurs for frequencies ω exclusively in one set of frequencies.

$\{\varepsilon_x, \varepsilon_y, \varepsilon_z\}$	r_p	r_s
$\{\varepsilon_\perp, \varepsilon_\perp, \varepsilon_\parallel\}$ (c-plane)	$\cup_{i=1..3} \{\omega_{TO}, \omega_{LO}\}_{\perp,i} \setminus \{\omega_{LO}, \omega_{LO^*}\}_\parallel$	$\cup_{i=1..3} \{\omega_{TO}, \omega_{LO^*}\}_{\perp,i}$
$\{\varepsilon_\parallel, \varepsilon_\perp, \varepsilon_\perp\}$ (a-plane) $c \parallel x$	$\cup_{i=1..3} \{\omega_{TO}, \omega_{LO}\}_\parallel \setminus \{\omega_{LO}, \omega_{LO^*}\}_{\perp,i}$	$\cup_{i=1..3} \{\omega_{TO}, \omega_{LO^*}\}_{\perp,i}$
$\{\varepsilon_\perp, \varepsilon_\parallel, \varepsilon_\perp\}$ (a-plane) $c \perp x$	$\cup_{i=1..3} \{\omega_{TO}, \omega_{LO^*}\}_{\perp,i}$	$\{\omega_{TO}, \omega_{LO^*}\}_\parallel$

TABLE II. Room temperature transverse and longitudinal optical phonon mode frequency parameters for rutile TiO_2 in units of cm^{-1}. Frequency parameters for additional modes included in the analysis are also given.

	Eagles[a] (Ref. [36])		Traylor *et al.*[b] (Ref. [13])		Gervais and Piriou[c] (Ref. [9])		This work	
	ω_{TO}	ω_{LO}	ω_{TO}	ω_{LO}	ω_{TO}	ω_{LO}	ω_{TO}	ω_{LO}
E_u								
1	183	373	188.8 ± 2.5	374.7 ± 3.7	189	367	188.6±1.2	365.7±0.2
2	388	458	not found	428.7 ± 4.3	381.5	443.5	379.3±0.2	444.9±0.2
3	500	806	494.0 ± 5.07	841.9 ± 11.3	508	831	500.5±0.3	829.6±0.3
A_{2u}								
	167	811	172.7 ± 1.7	not found	172	796	172.3±1.9	796.5±0.5
Additional modes								
$\varepsilon_{\perp,1}$					585	575	556±5	549±6
$\varepsilon_{\perp,2}$							781±15	780±15
$\varepsilon_{\parallel,1}$					592	589.5	587±12	584±15
$\varepsilon_{\parallel,2}$							710±18	709±20

[a]Reanalyzed IR reflectivity data by Spitzer *et al.* (Ref. [8]), assuming fixed values for ε_∞ and ε_0. No data for match of experimental and model data were shown, classic harmonic oscillator approach applied.
[b]Determined by neutron scattering.
[c]Determined from IR reflectivity data by applying FPSQ model.

ellipsometer in the spectral range between $300\,cm^{-1}$ and $650\,cm^{-1}$. The data points are nearly indistinguishable and demonstrate the comparable accuracy of both instruments. In order to achieve the presented excellent agreement between experimental and best-match model calculated data, a MDF of the factorized form in Eq. (12) was applied. The energetic position of the symmetry-predicted transverse and longitudinal phonon modes is indicated by brackets for which the solid lines indicate TO and the dashed lines LO phonons. The phonon mode parameters as determined from the regression analysis are summarized in Tables II–IV.

The Ψ and $\cos\Delta$ spectra show sharp features within the reststrahlen range. These features are related to the bands of total reflection for *p*- and *s*-polarized light components between the E_u and A_{2u} phonon modes. The anisotropic reflectivity in the uniaxial TiO_2 causes narrow structures, which directly point to LO phonon energies. The rules for identification of these bands of total reflection for *p*- and *s*-polarized light were described in the theory section and are summarized in Table I for the highly symmetric sample orientations investigated here. To assist the reader in understanding the ellipsometry data, the simulated bands of total reflection for *p*- and *s*-polarized light according to the determined best-matching phonon mode energies (Table II) are given in Figs. 2–4. The data are plotted as a function of the angle of incidence Φ_a, and broadening is omitted for the calculations. Figures 2 and 3 contain the *p* and *s* bands for the *c*-plane [four bands for r_p (a) and three bands for r_s (b)] and the *a*-plane surfaces [four bands for r_p at $c \parallel x$ (a) and one band for r_s at $c\perp x$ (b)]. As pointed out in Table I, the bands of total reflection of *s*-polarized light for an *a*-plane sample

TABLE III. Room temperature transverse and longitudinal optical phonon mode broadening parameters for rutile TiO_2 in units of cm^{-1}. Broadening parameters for additional modes included in the best-matching model are also given.

	Gervais and Piriou[a]		This work	
	γ_{TO}	γ_{LO}	γ_{TO}	γ_{LO}
E_u				
1	27	10	14.7 ± 8.0	8.8 ± 1.8
2	16.5	21.5	19.3 ± 2.8	18.4 ± 2.2
3	24	50	22.4 ± 3.1	43.9 ± 3.4
A_{2u}				
	76[b]	38[b]	20.0 ± 10.2	46.4 ± 5.3
Additional modes				
$\varepsilon_{\perp,1}$	55	55	64.7 ± 1.2	57.8±2.4
$\varepsilon_{\perp,2}$			77.1 ± 5.4	70.4 ± 4.8
$\varepsilon_{\parallel,1}$	65	65	56.2 ± 4.6	52.0 ± 4.2
$\varepsilon_{\parallel,2}$			68.7 ± 7.6	74.9 ± 8.2

[a]Determined from IR reflectivity data by applying FPSQ model.
[b]Note that Lowndes condition is not fulfilled for phonon modes of A_{2u} symmetry.

TABLE IV. Low-frequency ("static") and high-frequency dielectric constants of rutile TiO_2 at room-temperature.

	$\varepsilon_{\perp,0}$	$\varepsilon_{\perp,\infty}$	$\varepsilon_{\parallel,0}$	$\varepsilon_{\parallel,\infty}$
This work	84.69[a]	5.96 ± 0.03	152.97[a]	7.16 ± 0.03
DeVore[b]	84.02[a]	5.91[b]	153.83[a]	7.19[b]
Gervais and Piriou[c]	81.8[d]	6.0[c]	167.1[d]	7.8[c]
Klein *et al.*[e]	87[e]	6.12[a]	163[e]	7.63[a]
Samara and Percy[f]	89.8[f]	6.32[a]	166.7[f]	7.80[a]

[a]Calculated by using the LST relation, phonon modes as obtained in this work.
[b]Reference [1], minimum deviation method for prisms cut from bulk single crystals.
[c]Reference [10], IR reflectivity, note that $\varepsilon_{\parallel,\infty}$ is much larger than measured values by other authors in near-IR to visible spectral range resulting in larger calculated $\varepsilon_{\parallel,0}$ values (Refs. [1], [21], and [22]).
[d]Calculated by using the LST relation, phonon modes as obtained in Reference [10].
[e]Reference [17], microwave resonator at 200 GHz.
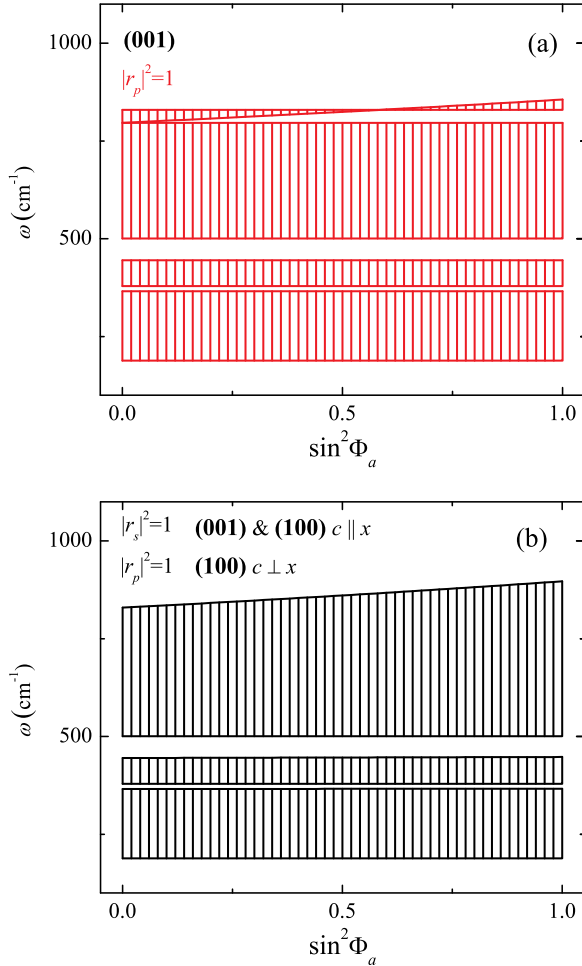[f]Reference [14], capacitance measurements at 100 kHz.

FIG. 2. Calculated bands of total reflection for p- (a) and s-polarized light (b) for c-plane rutile TiO_2 as a function of $k_x^2 = \sin^2\Phi_a$ (hatched areas). The data in (b) are also representing the bands of total reflection of s-polarized light for an a-plane sample with $c \parallel x$ and of p-polarized light for an a-plane sample with $c \perp x$.
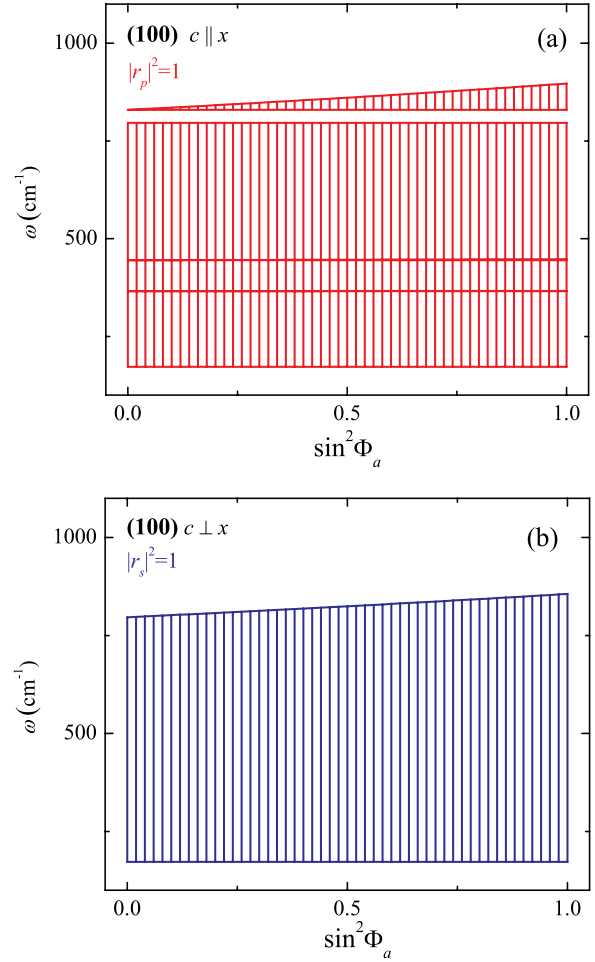
FIG. 3. Same as Fig. 2 for a-plane rutile TiO_2 as a function of $k_x^2 = \sin^2\Phi_a$ (hatched areas). (r_p at $c \parallel x$ and r_s at $c \perp x$). The bands of total reflection for r_s at $c \parallel x$ and r_p at $c \perp x$ are identical to those of r_s in Fig. 2(b).

at $c \parallel x$ and of p-polarized light for an a-plane sample at $c \perp x$ are identical to the data for s-polarized light on a c-plane surface in Fig. 2(b). Due to the k_x-dependence of the frequencies ω_{LO*i}, the high-frequency edges of the reflectivity bands at $(A_{2u})\omega_{LO*}$ in Figs. 2(a) and 3(b) and $(E_u)\omega_{LO*3}$ in Figs. 2(b) and 3(a) shift as a function of Φ_a from $(A_{2u})\omega_{LO}$ and $(E_u)\omega_{LO3}$ ($\Phi_a = 0°$) to $(A_{2u})\omega_{LO*}$ and $(E_u)\omega_{LO*3}$, at which $\varepsilon_\parallel(\omega_{LO*}) = \varepsilon_\perp(\omega_{LO*3}) = 1$ ($\Phi_a = 90°$). The crossover of the high-frequency p-reflectivity edge in Fig. 2(a) at $\Phi_a \sim 50°$ occurs where $(A_{2u})\omega_{LO*}$ equals $(E_u)\omega_{LO3}$. In Fig. 3(a), the frequency ranges $(E_u)\{\omega_{LO1}, \omega_{LO*1}\}$ and $(E_u)\{\omega_{LO2}, \omega_{LO*2}\}$ cut the $(A_{2u})\{\omega_{TO}, \omega_{LO}\}$ band into three bands. $(E_u)\omega_{LO*1}$ and $(E_u)\omega_{LO*2}$ vary insignificantly as a function of Φ_a. Therefore, except for the high-frequency edges, the upper boundaries for the reflection bands in Fig. 2(b) and lower boundaries in Fig. 3(a) appear almost independent of Φ_a at the frequencies ω_{LO*i}.

Figures 4(a)–4(c) show the calculated p- and s-reflection coefficient spectra for the highly symmetric orientations of the c-plane surface and a-plane surface of rutile TiO_2 at $\Phi_a = 72°$. The data were calculated by using the dielectric functions $\varepsilon_\parallel$ and $\varepsilon_\perp$ obtained in this work. Broadening was omitted for clarity. The spectral regions in which $|r_p|^2$ and
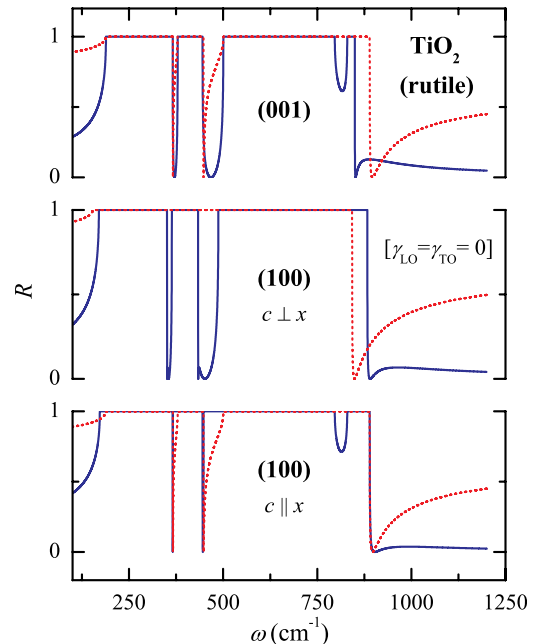

FIG. 4. Calculated p- (solid) and s-polarized light reflection coefficients (dotted lines) at an angle of incidence of 72° for high-symmetry orientations of rutile TiO_2: (a) c-plane, (b) a-plane, $c \perp x$, (c) a-plane, $c \parallel x$. The data were calculated by using the dielectric functions $\varepsilon_\parallel$ and $\varepsilon_\perp$ obtained in this work and neglecting broadening for clarity.

$|r_s|^2$ equal unity are equal to the reststrahlen bands discussed above. Outside the reststrahlen ranges, r_p and r_s drop to very small values. Ψ and $\cos\Delta$ show very sharp features in regions of spectral delay between minima in r_p and r_s. At the high-frequency edge of the reststrahlen bands, dielectric loss occurs when the DF approaches unity causing the reflection coefficients to drop to zero. Spectral delay of this loss for p- and s-polarized light results in derivative-like structures in the ellipsometry spectra.

By combining the information from Tables I and II, as well as Figs. 2 and 4, the experimental data in Fig. 1 can be related to the phonon modes of rutile TiO_2. In the lower frequency range, total p- and s-reflection occurs between (E_u) $\omega_{TO1}(188.61 \text{ cm}^{-1})$ and $(E_u)\omega_{LO1}(365.74 \text{ cm}^{-1})$ where $\Psi \sim 45°$. The drop of Ψ for $\omega > (E_u)\omega_{TO1}$ is related to the drop in p reflectivity. The sample is totally reflecting p- and s-light again in the frequency ranges (E_u) $\omega_{TO2}(379.27 \text{ cm}^{-1})$ to $(E_u)\omega_{LO2}(444.91 \text{ cm}^{-1})$ and (E_u) $\omega_{TO3}(500.46 \text{ cm}^{-1})$ to $(A_{2u})\omega_{LO}(796.51 \text{ cm}^{-1})$, but Ψ does not reach $45°$ due to broadening and the existence of symmetry-forbidden additional modes (see discussion below). Ordinary and extraordinary dielectric functions approach unity at different energetic positions. The related loss in p- and s-polarized reflectivities causes the derivative-like structure in Ψ near 900 cm^{-1}. The order of the minimum and maximum of this derivative-like structure indicates whether the uniaxial material is positive or negative birefringent for photon energies near the reststrahlen band region. Rutile TiO_2 is positive uniaxial in this spectral range, i.e., $\varepsilon_\parallel > \varepsilon_\perp$.

Figure 5 shows the same data as discussed above, but for an a-plane surface for which the c-axis is oriented parallel to the plane of incidence ($c \parallel x$). Tables I and II in combination with Figs. 2(b)–4 help to understand the main features. The two prominent peaks in the middle of the reststrahlen range of the Ψ spectrum are related to the anisotropy of rutile TiO_2 ($\Psi > 45°$). The reflection coefficient r_p only deviates from unity in the wide frequency range (A_{2u}) $\{\omega_{TO}(172.37 \text{ cm}^{-1}), \omega_{LO}(796.51 \text{ cm}^{-1})\}$ for the very narrow frequency ranges $(E_u)\{\omega_{LO1} (365.74 \text{ cm}^{-1}), \omega_{LO*1} (366.38 \text{ cm}^{-1})\}$ and (E_u) $\{\omega_{LO2}(444.91 \text{ cm}^{-1}), \omega_{LO*2} (447.35 \text{ cm}^{-1})\}$, while losses in s reflectivity occur in the wider frequency ranges (E_u) $\{\omega_{LO*1}(366.38 \text{ cm}^{-1}), \omega_{TO2} (379.27 \text{ cm}^{-1})\}$ and (E_u) $\{\omega_{LO*2}(447.35 \text{ cm}^{-1}), \omega_{TO3} (500.46 \text{ cm}^{-1})\}$. Since Ψ is related to the ratio r_p/r_s, a drop in s-reflectivity causes peak-like features in the Ψ spectrum.

The Ψ and $\cos\Delta$ spectra for an a-plane surface with c-axis orientation perpendicular to the plane of incidence ($c \perp x$) is shown is Fig. 6. The reflection coefficient r_s equals unity over the whole spectral range between $(A_{2u})\omega_{TO}$ (172.37 cm^{-1}) and $(A_{2u})\omega_{LO*}(849.34 \text{ cm}^{-1})$. Drops in p-reflectivity occur in the frequency ranges $(E_u)\{\omega_{LO*1} (366.38 \text{ cm}^{-1}), \omega_{TO2}(379.27 \text{ cm}^{-1})\}$ and $(E_u)\{\omega_{LO*2} (447.35 \text{ cm}^{-1}), \omega_{TO3} (500.46 \text{ cm}^{-1})\}$ causing the dips in Ψ and peaks in $\cos\Delta$. r_p remains unity between $(E_u)\omega_{TO3}$ (500.46 cm^{-1}) and $(E_u)\omega_{LO3}(889.11 \text{ cm}^{-1})$. The spectral delay between p- and s-reflectivities loss results in the peak in Ψ around 900 cm^{-1}.

Within the IR dielectric response, critical point structures similar to those for direct electronic band-band transitions in the near-IR-UV spectral range occur when the polarization
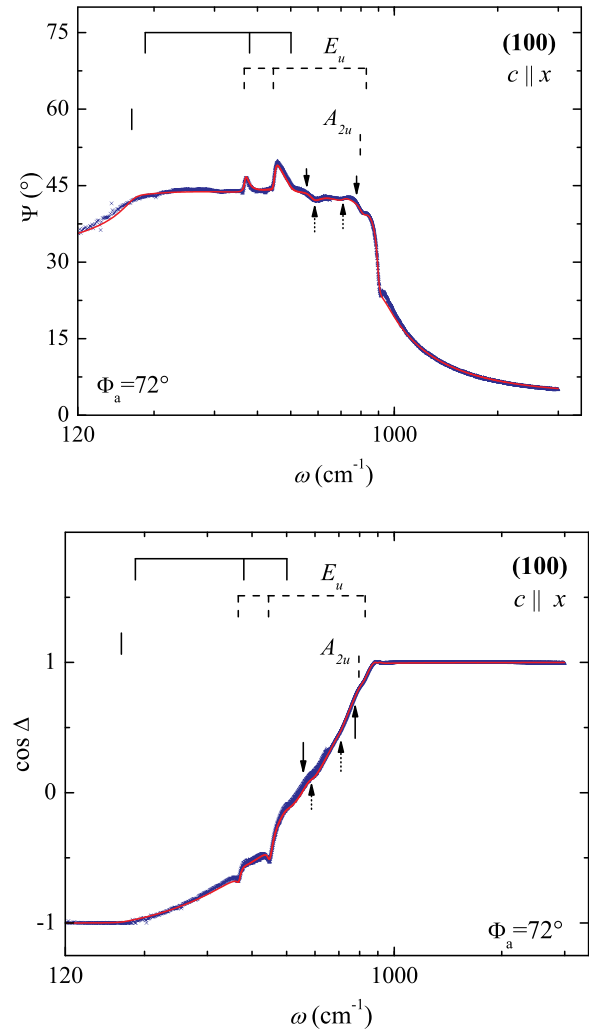

FIG. 5. Same as Fig. 1 for an a-plane sample of rutile TiO_2 for which the c-axis is oriented in the plane of incidence ($c \parallel x$).

and photon energy of the incident light matches conditions for which the lattice vibration of a polar phonon mode can be driven by the electromagnetic wave. Second-derivative spectra of the pseudo-dielectric function provide sensitivity for these critical point structures in the case of crystalline substrates as investigated here. Experimental and best-matching model calculated data of the second derivative of the pseudo-dielectric function $d^2\langle\varepsilon\rangle/dE^2$ for the c-plane sample is given in Fig. 7.[37] Experimental and best-matching model calculated data are in excellent agreement even for the derivatives presented here. Strong resonance structures occur at the phonon mode frequencies $(E_u)\omega_{TO1}$ and $(E_u)\omega_{TO2}$. Less pronounced structures are apparent between the phonon mode frequencies $(A_{2u})\omega_{LO}$ and $(E_u)\omega_{LO3}$ marked by arrows around 800 cm^{-1} in the inset of Fig. 7. Further, structures related to additional modes are highlighted (see discussion below). The resonance-like structure around 900 cm^{-1} is related to the minima in p- and s-reflectivities, respectively.

The imaginary part of the second derivative for both high-symmetry orientations of the a-plane sample are presented in Fig. 8. Except for the missing derivative-like structure between $(A_{2u})\omega_{LO}$ and $(E_u)\omega_{LO3}$, the spectrum for $c \perp x$ is very similar to the one for c-plane orientation. For c-axis
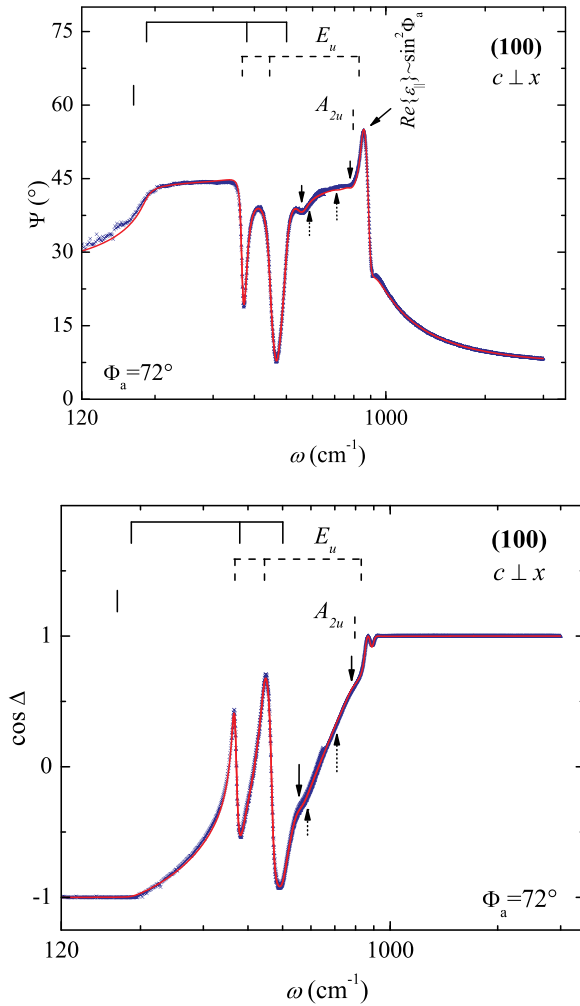
FIG. 6. Same as Fig. 1 for an *a*-plane sample of rutile TiO₂ for which the *c*-axis is oriented perpendicular to the plane of incidence ($c \perp x$).
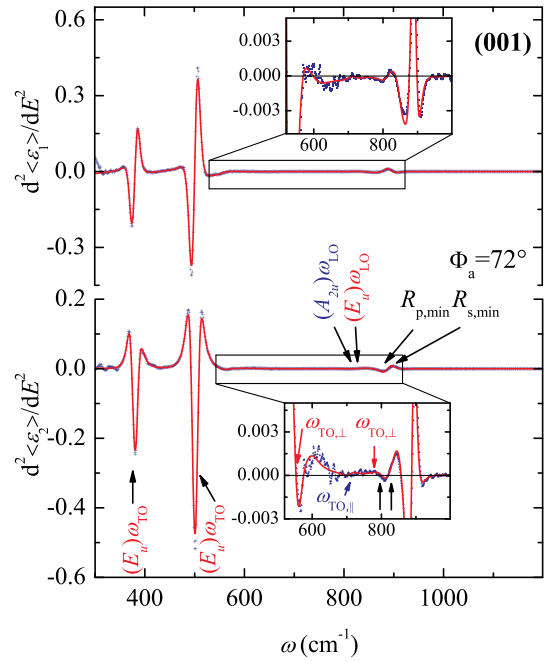

FIG. 7. Experimental (symbols) and best-matching model calculated (solid lines) real and imaginary part of the second derivative of the pseudo-dielectric function $d^2\langle\varepsilon\rangle/dE^2$ for *c*-plane rutile TiO₂. Critical point structures related to phonon modes are marked by arrows. The inset magnifies the spectral range between $520\,\mathrm{cm}^{-1}$ and $1000\,\mathrm{cm}^{-1}$. The position and type of additional modes are also indicated in the inset. The derivative-like structure near $900\,\mathrm{cm}^{-1}$ is caused by the subsequent loss in *p*- and *s*-reflectivity above the reststrahlen range.

orientation parallel to the plane of incidence ($c \parallel x$), derivative-like structures occur at $(E_u)\omega_{\mathrm{LO}^*1}$ and $(E_u)\omega_{\mathrm{LO}^*2}$. The same derivative-like structure between the phonon mode frequencies $(A_{2u})\omega_{\mathrm{LO}}$ and $(E_u)\omega_{\mathrm{LO}3}$ as seen for the *c*-plane sample is also present for $c \parallel x$. Resonance structure due to subsequent loss of *s*- and *p*-reflectivities are apparent in both cases $c \perp x$ and $c \parallel x$.

As mentioned above, additionally to the symmetry-predicted one phonon mode pair of A_{2u}-symmetry and three phonon mode pairs of E_u-symmetry, two additional modes were included for each model dielectric function tensor component in order to improve the match between model and experimental data. The energetic positions of these additional modes are indicated in Figs. 1, 5, and 6. Signatures of these four additional modes are present in measurements of all surface orientations and also cause derivative-like features in the second derivatives of the pseudo-dielectric functions in Figs. 7 and 8. In order to determine if an additional mode structure occurs in $\varepsilon_\parallel$ or $\varepsilon_\perp$ and to evaluate the quality of our parameterized model compared to wavelength-by-wavelength determined dielectric function tensor components, a simultaneous point-by-point fit for the measurements of all highly symmetric sample orientations was performed.
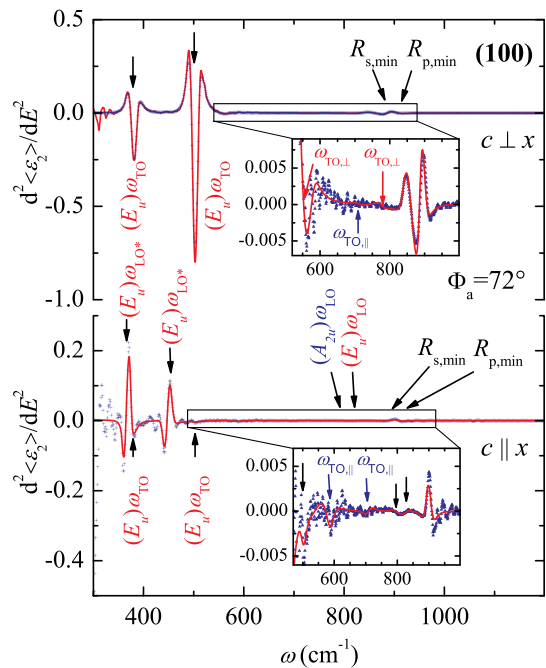

FIG. 8. Experimental (symbols) and best-matching model calculated (solid lines) imaginary part of the second derivative of the pseudo-dielectric function $d^2\langle\varepsilon_2\rangle/dE^2$ for *a*-plane rutile TiO₂ with *c*-axis oriented perpendicular ($c\perp x$) and parallel to the plane of incidence ($c \parallel x$). Critical point structures related to phonon modes are marked by arrows. The inset magnifies the spectral range between $520\,\mathrm{cm}^{-1}$ and $1000\,\mathrm{cm}^{-1}$. The position and type of additional modes are also indicated in the inset. The derivative-like structure near $900\,\mathrm{cm}^{-1}$ is caused by the subsequent loss in *s*- and *p*-reflectivity above the reststrahlen range.
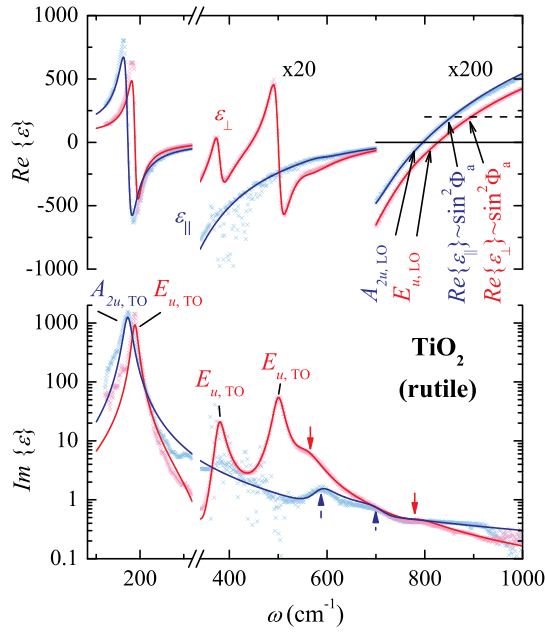
FIG. 9. Comparison of the real and imaginary part of the dielectric function tensor components $\varepsilon_\parallel$ and $\varepsilon_\perp$ of rutile TiO$_2$ as determined by applying the parameterized MDF in Eq. (12) (solid lines) and a point-by-point fit (symbols) determined in a simultaneous analysis of a *c*-plane oriented sample and an *a*-plane oriented sample measured at highly symmetric sample orientations ($c\perp x$ and $c\parallel x$). The energetic position of TO phonons, the high-frequency edge zero-crossing of the real part of $\varepsilon_\parallel$ and $\varepsilon_\perp$ (highest-frequency LO phonons), and the positions for which $\varepsilon_\parallel$ and $\varepsilon_\perp$ equal $k_x^2 = \sin^2 \Phi_a$ (LO*) are indicated by markers. Features caused by additional modes are highlighted by arrows. Note the excellent agreement between model dielectric function and point-by-point fit even in the range of additional modes.

Such a point-by-point fit procedure does not imply a certain lineshape following a preselected physical model, and therefore can highlight subtle features often overseen in MDF approaches. A comparison of the best-match MDF tensor components and the point-by-point extracted DF tensor components is presented in Fig. 9. Maxima in the imaginary part of $\varepsilon_\parallel$ and $\varepsilon_\perp$ represent the energetic position of the TO phonons. Signatures of additional modes are clearly present in both dielectric function tensor components (marked by arrows). Excellent agreement between parameterized model dielectric function and point-by-point fit even in the range of these additional modes was achieved. The energetic position of LO phonons is equivalent to the maximum positions in the imaginary part of the dielectric loss function $1/\varepsilon$, which is plotted in Fig. 10 for both dielectric function tensor components. Gervais and Piriou also reported two additional modes for their rutile TiO$_2$ sample (see Table II).[10] The reported mode frequencies are in the range of the lower-frequency additional mode found in this study. We expect that the reported modes and the modes found in this study have the same origin, however, due to the much lower spectral resolution, Gervais and Piriou might not had sufficient sensitivity to observe other additional modes and to localize the spectral position of the reported modes more precisely. To our knowledge, there are no studies in literature that specify a possible origin of these additional modes. X-ray diffraction measurements did not indicate structural distortions that would indicate a lowering of the overall crystal symmetry.
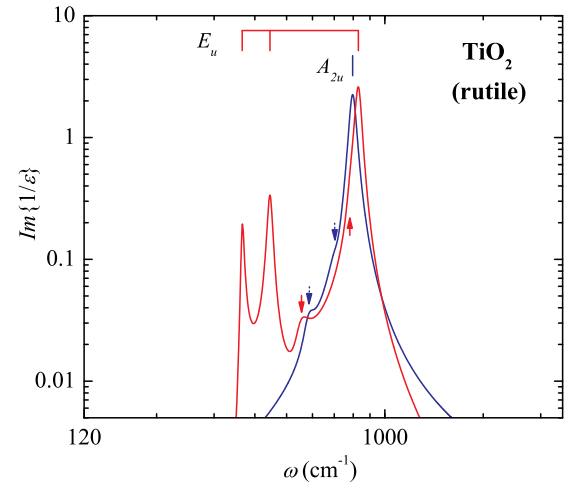

FIG. 10. Imaginary part of the dielectric loss functions $1/\varepsilon_\perp$ and $1/\varepsilon_\parallel$ as determined form the parameterized model dielectric function analysis. The position of LO phonons coincides with the maximum positions and is indicated by brackets. Signatures related to additional modes are marked by arrows.

Spectral features for the same additional modes were found in all investigated surface orientations. Therefore, surface reconstruction effects can be excluded as an origin for these symmetry-forbidden modes.

To further narrow down possible origins of the additional modes, density functional theory (DFT) calculations were performed. We have used the DFT-based plane-wave method *Quantum Espresso* (QE)[38] and Vanderbilt ultrasoft pseudopotentials[39] for the relaxation of ionic positions and stress tensor components $\sigma_{\alpha\beta}$ (with the tetragonal symmetry enforced) of the simulation cell. The phonon frequencies were computed with the help of a density-functional perturbation theory (DFPT) approach.[40] The exchange-correlation interaction was described by the local-density approximation functional of Perdew and Zunger.[41] The electronic wave-function and density plane-wave cutoffs were 50 and 500 Ry, respectively. The system was considered to be at equilibrium when the forces on the ions were less than 1.0×10^{-4} Ry/bohr (~ 0.003 eV/Å), and the $\sigma_{\alpha\alpha}$ components of the stress tensor were smaller than 0.06 kbar. Brillouin-Zone integrations and phonon-band dispersion calculations were done over a $4 \times 4 \times 6$ and a $3 \times 3 \times 3$ Monkhorst-Pack grid, respectively.[42] The resulting phonon mode dispersion and phonon DOS are presented in Fig. 11 in comparison to the position of our determined phonon modes. The positions of the additional modes are indicated by horizontal lines. The calculated positions of the IR-active phonon modes at the Γ-point match well with the experimentally determined modes. The positions of the additional modes are found to be close to maxima in the phonon DOS. These results allow the interpretation that phonon modes off the Γ-point become IR-active due to defects in the crystal. Apart from off-Γ-point modes, defect atoms might also cause the formation of local modes in the host lattice, which would depend on the specific type of impurity. Further structural investigations are required to characterize these defects, but go beyond the scope of this article.
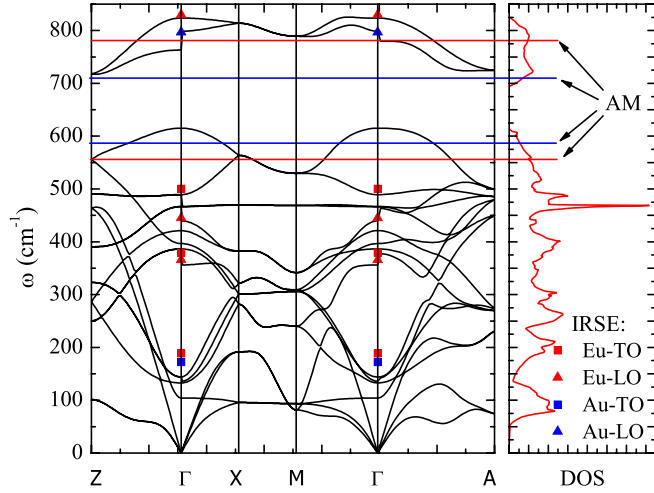
FIG. 11. Phonon dispersion and phonon density of states of rutile TiO$_2$ as determined by DFT calculations. The spectral positions of the phonon modes at the Γ-point determined by IR spectroscopic ellipsometry are marked by squares (TO modes) and triangles (LO modes). The spectral positions of additional modes are marked by horizontal lines.
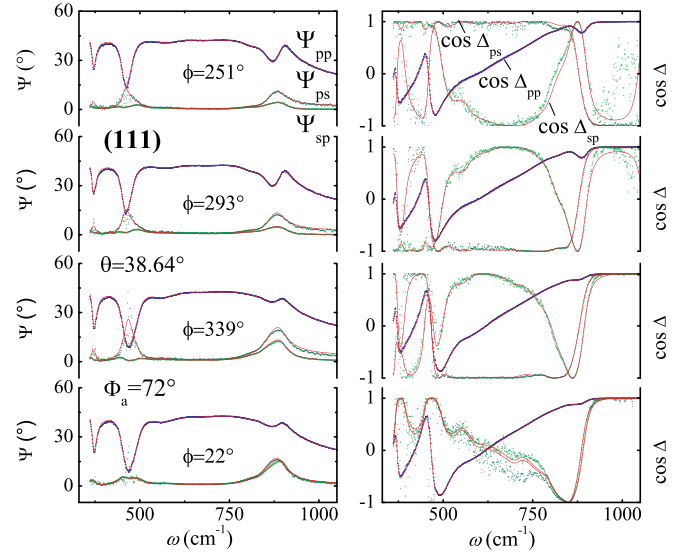

FIG. 12. Experimental (symbols) and best-matching model calculated data (solid lines) of the ellipsometric parameters Ψ and cosΔ in the Jones-matrix representation for rutile TiO$_2$ sample of (111) orientation measured at four different in-plane orientations at an angle of incidence $\Phi_a = 72°$. The model data were calculated by applying the determined phonon mode parameters without further regression analysis. Only the Euler angles for in-plane orientation φ and tilt of the c-axis with respect to the z-axis of the laboratory coordinate system θ were varied during the model analysis. Excellent agreement even for the off-diagonal Jones-matrix elements was achieved.

The line width of the absorption peaks in the imaginary parts of the DF and dielectric loss function is related to the phonon broadening parameters γ, which are summarized in Table III. The peaks in the DF and dielectric loss functions in Figs. 9 and 10 are clearly non-symmetric. In order to maintain the physical meaning of ε, i.e., the imaginary part of ε is positive over the whole measured spectral range, the broadening parameters must fulfill the generalized Lowndes condition derived by Schubert *et al.*:[23] $\sum(\gamma_{LOi} - \gamma_{TOi}) > 0$. The determined best-match model broadening parameters including broadening parameters for the additional modes are summarized in Table III. If the additional modes are neglected, we find $(A_{2u})\sum(\gamma_{LO} - \gamma_{TO}) = 26.37\,\mathrm{cm}^{-1}$ and $(E_u)\sum(\gamma_{LOi} - \gamma_{TOi}) = 14.69\,\mathrm{cm}^{-1}$. If the additional modes are included, $(A_{2u})\sum(\gamma_{LO} - \gamma_{TO}) = 28.26\,\mathrm{cm}^{-1}$ and $(E_u)\sum(\gamma_{LOi} - \gamma_{TOi}) = 1.13\,\mathrm{cm}^{-1}$ are determined. Generally, positive values of the imaginary parts of $\varepsilon_\parallel$ and $\varepsilon_\perp$ are verified throughout the whole measured spectral range. Note that the generalized Lowndes condition is not fulfilled for the phonon modes of A_{2u} symmetry reported by Gervais and Piriou.[10]

The parameterized best-match MDF was applied to match experimental data obtained for a rutile TiO$_2$ sample of arbitrary c-axis orientation. Measurements were taken in the generalized ellipsometry mode for a sample of (111) surface orientation. Four different in-plane orientations were investigated between which the sample was rotated manually by approximately 45°. The resulting experimental and best-matching model calculated data is shown in Fig. 12. During the model analysis, the determined phonon mode parameters were kept fixed and only the Euler angles for in-plane orientation φ and tilt of the c-axis with respect to the z-coordinate of the laboratory coordinate system θ were allowed to be varied in order to match the experimental data set as close as possible. Since the c-axis tilt compared to the surface normal is a sample property that does not change with in-plane rotation, the θ angle was coupled for all measured sample

orientations. Excellent agreement for all Jones-matrix elements was achieved. A tilting angle $\theta = 38.6° \pm 0.2°$ was determined, which is consistent with the results obtained for this sample by generalized ellipsometry in the near-IR-vacuum-ultraviolet spectral range $(40.5° \pm 0.5°)$[20,22] and by X-ray diffraction $(42° \pm 3°)$. The model results for the in-plane orientations for each measurement are given in Fig. 12.

The static and high-frequency dielectric constants as obtain in this work in comparison to existing literature values are given in Table IV. The high-frequency dielectric constant ε_∞ is a parameter obtained in our MDF (Eq. (12)). The static dielectric constant ε_0 is calculated by applying the LST relation (Eq. (14)). In the same way, by using our determined phonon mode parameters, high-frequency dielectric constants can be calculated for measured low-frequency dielectric constants from literature. The high-frequency dielectric constants obtained in this work are matching the values found by DeVore for measurements of the minimum deviation of light in prisms of different crystal orientation cut from bulk single crystals.[1] The optical constants determined by generalized ellipsometry in the near-IR to ultra-violet spectral range by Tiwald and Schubert for the same sample investigated in this study[22] and by Jellison *et al.*[21] match the optical constants found by DeVore proving the accuracy of the high-frequency dielectric constants determined here. Our calculated low-frequency dielectric constants are in the same range as the ones determined at low frequencies by capacitance measurements at 100 kHz (Ref. 14) and on microresonators at 200 GHz.[17] However, slightly smaller values are determined for both DF tensor components, i.e., $\varepsilon_{\parallel,0}$ and $\varepsilon_{\perp,0}$. The larger static values obtained by the GHz and kHz measurements indicate that there might be additional,

defect-induced, small-polarity modes in the acoustic regions of the phonon mode spectrum, which was not measured in this work. Further, slight discrepancy can be caused by small deviations of the phonon mode frequencies used for the calculation of ε_0. For example, ordinary and extraordinary TO mode frequencies in the far-IR in our analysis are slightly less certain than those in the mid-IR spectral range due to larger experimental errors. Also, the uncertainty values of the phonon mode parameters for phonons of A_{2u} symmetry are slightly larger than for those of E_u symmetry (see Tables II and III). If the largest error for the parameters in the LST calculations is assumed, maximum values of $\varepsilon_{\perp,0} = 86.65$ and $\varepsilon_{\parallel,0} = 157.34$ are obtained from our results, which are still slightly smaller than the reported values. The low-frequency dielectric constants determined by IR reflectivity by Gervais and Piriou are less consistent. The value of the ordinary component $\varepsilon_{\perp,0}$, calculated by applying the LST relation and phonon mode frequencies as determined by Gervais and Piriou, is much smaller than values actually determined at low frequencies by others, while the extraordinary component $\varepsilon_{\parallel,0}$ matches very well. However, Gervais and Piriou report a high-frequency dielectric constant $\varepsilon_{\parallel,\infty}$ that is significantly higher than experimentally determined values. Using the high-frequency dielectric constant $\varepsilon_{\parallel,\infty}$ by DeVore for the calculation results in a low-frequency dielectric constant $\varepsilon_{\perp,0} = 153.78$, which agrees well with our value.

Figure 13 summarizes the optical function data within the IR spectral range for the ordinary ($[n_\perp + ik_\perp] = \sqrt{\varepsilon_\perp}$) and the extraordinary ($[n_\parallel + ik_\parallel] = \sqrt{\varepsilon_\parallel}$) optical functions. Solid lines represent the optical functions determined in this work. Symbols refer to room temperature data taken from literature.[43] For wavelengths below 15 μm, most data points coincide. Above, larger disagreement is found for the refractive index values indicating discrepancy of the absorption coefficients in the long wavelengths range. We believe that the investigation presented here resulted in more accurate optical functions of rutile TiO_2 and attribute the discrepancy
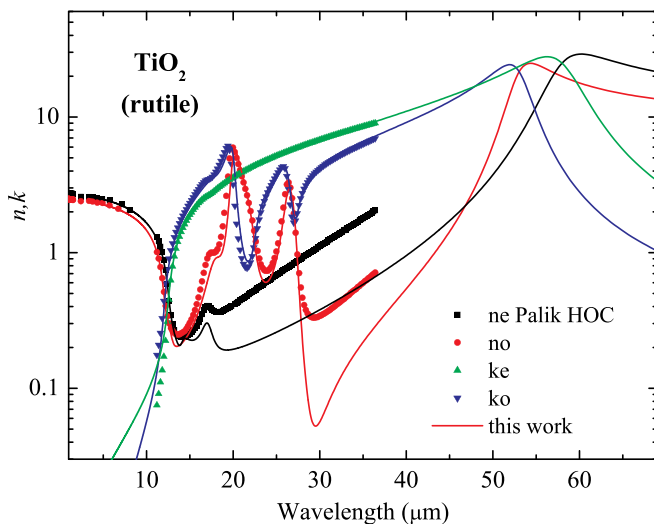
to uncertainties in the reflectivity and K-K inversion obtained optical functions in former studies and disregard of Lowndes rule.

V. CONCLUSIONS

A comprehensive study of the IR dielectric response function of rutile TiO_2 was performed in the far-IR and mid-IR spectral range by applying standard and generalized spectroscopic ellipsometry. By employing the four-parameter semiquantum model derived by Gervais and Piriou, the parameters frequency and broadening for all IR-active LO and TO phonon modes of rutile were determined. The extracted phonon mode frequencies were found in excellent agreement with existing literature values. The determined anharmonic broadening parameters were shown to be in agreement with a generalized Lowndes condition. Conditions for total reflection of p- and s-polarized light for highly symmetric orientations of rutile TiO_2 were derived and bands of total reflection in dependence of the angle of incidence were given. These data were used to explain the spectral features in the standard ellipsometry measurements for the highly symmetric sample orientations. Critical point-like structures in the pseudo-dielectric function were identified and explained. The dielectric function as determined from the model analysis is compared to a point-by-point extracted dielectric function. Two additional modes for each dielectric function tensor component are included to further improve the match between model and experimental data, and their spectral positions are compared to phonon density of state calculations. Defect-activated off-Γ-point phonon modes are found as a possible origin for these modes. The best-matching model extracted dielectric function was applied without further regression analysis to excellently match experimental generalized ellipsometry data taken on four orientations of a rutile TiO_2 sample of arbitrary c-axis orientation. The Euler angles for this sample were determined and found in excellent agreement with previously reported values. The determined high-frequency dielectric constants match the values reported for investigations in the near-IR to visible spectral range. The calculated low-frequency dielectric constants are close to experimentally determined low-frequency dielectric constants. Our reported optical functions revise existing literature optical functions and are believed to be more accurate. The dielectric functions of rutile TiO_2 can easily be calculated by using the four-parameter semiquantum model and our reported phonon mode parameters and will be very useful for IR analysis of bulk TiO_2 single crystal substrates, thin films, and TiO_2 nanostructures.

FIG. 13. Ordinary ($[n_\perp + ik_\perp] = \sqrt{\varepsilon_\perp}$) and extraordinary ($[n_\parallel + ik_\parallel] = \sqrt{\varepsilon_\parallel}$) room-temperature optical functions of rutile TiO_2. Symbols refer to room temperature data taken from literature.[43]

[1]J. DeVore, J. Opt. Soc. Am. **41**, 416 (1951).
[2]D. C. Cronemeyer, Phys. Rev. **113**, 1222 (1959).

[3]E. S. Sabisky and H. J. Gerritsen, J. Appl. Phys. **33**, 1450 (1962).

[4]M. Kadoshima, M. Hiratani, Y. Shimamoto, K. Torii, H. Miki, S. Kimura, and T. Nabatame, Thin Solid Films **424**, 224 (2003).

[5]J. Q. Xi, M. F. Schubert, J. K. Kim, E. F. Schubert, M. Chen, S. Y. Lin, W. Liu, and J. A. Smart, Nat. Photonics **1**, 176 (2007).

[6]B. O'Regan and M. Grätzel, Nature **353**, 737 (1991).

[7]U. Diebold, Surf. Sci. Rep. **48**, 53 (2003).

[8]W. G. Spitzer, R. C. Miller, D. A. Kleinman, and L. E. Howarth, Phys. Rev. **126**, 1710 (1962).

[9]F. Gervais and B. Piriou, J. Phys. C **7**, 2374 (1974).

[10]F. Gervais and B. Piriou, Phys. Rev. B **10**, 1642 (1974).

[11]F. Gervais and B. Piriou, Phys. Rev. B **11**, 3944 (1975).

[12]S. P. S. Porto, P. A. Fleury, and T. C. Damen, Phys. Rev. **154**, 522 (1967).

[13]J. G. Traylor, H. G. Smith, R. M. Nicklow, and M. K. Wilkinson, Phys. Rev. B **3**, 3457 (1971).

[14]G. A. Samara and P. S. Peercy, Phys. Rev. B **7**, 1131 (1973).

[15]P. D. Mitev, K. Hermansson, B. Montanari, and K. Refson, Phys. Rev. B **81**, 134303 (2010).

[16]R. A. Parker, Phys. Rev. **124**, 1719 (1961).

[17]N. Klein, C. Zuccaro, U. Dahne, H. Schulz, N. Tellmann, R. Kutzner, A. G. Zaitsev, and R. Wordenweber, J. Appl. Phys. **78**, 6683 (1995).

[18]M. E. Tobar, J. Krupka, E. N. Ivanov, and R. A. Woode, J. App. Phys. **83**, 1604 (1998).

[19]D. C. Cronemeyer, Phys. Rev. **87**, 876 (1952).

[20]M. Schubert, B. Rheinländer, J. A. Woollam, B. Johs, and C. M. Herzinger, J. Opt. Soc. Am. A **13**, 875 (1996).

[21]G. E. Jellison, Jr., F. A. Modine, and L. Boatner, Opt. Lett. **22**, 1808 (1997).

[22]T. E. Tiwald and M. Schubert, Proc. SPIE **4103**, 19 (2000).

[23]M. Schubert, T. E. Tiwald, and C. M. Herzinger, Phys. Rev. B **61**, 8187 (2000).

[24]P. S. Narayanan, Proc. Math. Sci. **32**, 279 (1950).

[25]C. M. Wolfe, N. Holonyak, and G. E. Stillmann, *Physical Properties of Semiconductors* (Prentice Hall, New Jersey, 1989).

[26]G. E. Jellison, Jr., Thin Solid Films **313–314**, 33 (1998).

[27]R. M. Azzam and N. M. Bashara, *Ellipsometry and Polarized Light* (North-Holland Publ. Co., Amsterdam, 1984).

[28]M. Schubert, Thin Solid Films **313–314**, 323 (1998).

[29]M. Schubert, Phys. Rev. B **53**, 4265 (1996).

[30]G. E. Jellison, Jr. and F. A. Modine, Appl. Opt. **36**, 8190 (1997).

[31]H. Fujiwara, *Spectroscopic Ellipsometry: Principles and Applications* (John Wiley & Sons Ltd, 2007).

[32]C. M. Herzinger, B. Johs, W. A. McGahan, J. A. Woollam, and W. Paulson, J. Appl. Phys. **83**, 3323 (1998).

[33]F. Gervais, Solid. State Commun. **13**, 1211 (1973).

[34]R. H. Lyddanne, R. G. Sachs, and E. Teller, Phys. Rev. **59**, 673 (1941).

[35]W. Cochran and R. A. Cowley, J. Phys. Chem. Solids **23**, 447 (1962).

[36]D. M. Eagles, J. Phys. Chem. Solids **25**, 1243 (1964).

[37]The second derivative value at each data point was obtained by fitting a second degree polynomial to 15 data points centered at the spectral frequency of interest. Note that the second-derivative data were not included in the regression analysis to determine the dielectric function and phonon mode parameters.

[38]See http://www.quantum-espresso.org for Quantum Espresso. See also, P. Giannozzi *et al.*, J. Phys.: Condens. Matter **21**, 395502 (2009).

[39]D. Vanderbilt, Phys. Rev. B **41**, 7892 (1990).

[40]S. Baroni, S. de Gironcoli, A. D. Corso, and P. Giannozzi, Rev. Mod. Phys. **73**, 515 (2001).

[41]J. P. Perdew and A. Zunger, Phys. Rev. B **23**, 5048 (1981).

[42]H. J. Monkhorst and J. D. Pack, Phys. Rev. B **13**, 5188 (1976).

[43]M. W. Ribarsky, "Titanium dioxide (TiO₂) (rutile)," in *Handbook of Optical Constants of Solids*, edited by E. D. Palik (Academic Press, San Diego, 1985), pp. 795–804.